

1 Laramide bulldozing of lithosphere beneath the Arizona
2 Transition Zone

3 Paul Kapp¹, Gilby Jepson², Barbara Carrapa¹, Allen J. Schaen¹, John J.Y. He¹, and Jordan
4 W. Wang¹

5 ¹*Department of Geosciences, University of Arizona, Tucson, Arizona 85721, USA*

6 ²*School of Geosciences, University of Oklahoma, Norman, Oklahoma 73019, USA*

7

8 **ABSTRACT**

9 **The northwest-trending Transition Zone (TZ) in Arizona is an ~100-km-wide**
10 **physiographic province that separates the relatively undeformed southwestern margin of**
11 **the Colorado Plateau from the hyperextended Basin and Range Province to the southwest.**
12 **The TZ is widely depicted to have been a Late Cretaceous – Paleogene northeast-dipping**
13 **erosional slope along which Proterozoic rocks were denuded but not significantly**
14 **deformed. Our multi-method thermochronological study (biotite ⁴⁰Ar/³⁹Ar, zircon and**
15 **apatite (U-Th-Sm)/He, and apatite fission-track) of Proterozoic rocks in the Bradshaw**
16 **Mountains of the west-central Arizona TZ reveals relatively rapid cooling (~10 °C/Myr)**
17 **from temperatures of >180 °C to <60 °C between ~70 and ~50 Ma. Given minimal ~70–50**
18 **Ma upper-crustal shortening in the TZ, we attribute cooling to exhumation driven by**
19 **northeastward bulldozing of continental lower crust and mantle lithosphere beneath it by**
20 **the Farallon flat slab. Bulldozing is consistent with contemporaneous (~70–50 Ma)**
21 **underplating and initial exhumation of Orocopia Schist to the southwest in western**

22 **Arizona and Mesozoic garnet-clinopyroxenite xenoliths of possible Mojave batholith keel**
23 **affinity in ~25 Ma TZ volcanic rocks.**

24

25 **INTRODUCTION**

26 An outstanding question in tectonics is the extent to which flat-slab oceanic subduction
27 beneath continental lithosphere can drive inboard translation and thickening of continental lower
28 crust. The anomalously thick crust of the Rocky Mountain foreland and Great Plains has been
29 attributed to inboard shearing of North American lithosphere by flat-slab subduction during the
30 Laramide (~85–40 Ma) orogeny (Bird, 1984). In the southwestern U.S., very shallow Laramide
31 flat-slab subduction is inferred to juxtapose subducted, mostly clastic sedimentary rocks
32 (Orocopia and related schists; henceforth Orocopia Schist) at depths of ~35 km beneath
33 continental crust over an inboard distance of ≥ 200 km (Fig. 1; Chapman, 2016; Jacobson et al.,
34 2017; Seymour et al., 2018). This hypothesis requires preexisting continental lower crust and
35 mantle lithosphere to have foundered into the mantle or been bulldozed inboard ahead of the
36 leading hinge in the flat slab (Axen et al., 2018; Chapman et al., 2020a).

37 The Transition Zone (TZ) in Arizona is a topographically rugged physiographic province
38 separating the southwestern Colorado Plateau from the Basin and Range Province (Fig. 1). The
39 TZ is transitional in the magnitude of Oligocene-Miocene extensional deformation, modern
40 crustal thickness (decreasing southwestward across it from ~45 km to ~25 km), and mean
41 elevation (Qashqai et al., 2016). The western TZ exposes 1.8–1.6 Ga (meta)granitic and
42 metasedimentary rocks, ~1.4 Ga plutons, and ~80–65 Ma tonalitic stocks (Fig. 2; DeWitt et al.,
43 2008). Proterozoic rocks are buried in places by Neogene syn- to post-extensional sedimentary
44 basins and volcanic rocks (DeWitt et al., 2008). The nonconformity between Proterozoic rocks

45 and Paleozoic strata is exposed in the northern TZ and dips regionally $<1-2^\circ$ to the northeast
46 (Fig. 1). The TZ was not significantly shortened during Laramide orogenesis (Jenney and
47 Reynolds, 1989), but became a proximal source of fluvial sandstone and conglomerate in
48 northwestern Arizona by ~ 64 Ma (Fig. 1; Young and Hartman, 2014; Hill et al., 2016). Recent
49 studies raise the possibility that continental lower crust and mantle lithosphere might have been
50 bulldozed beneath the TZ during Laramide flat-slab subduction (e.g., Chapman et al., 2020a).
51 The TZ is oriented nearly orthogonal to the $\sim 80-50$ Ma Farallon – North America relative plate
52 convergence vector (Fig. 1) and within the corridor where a hypothesized oceanic plateau
53 subducted beneath western North America (Livaccari et al., 1981; Saleeby, 2003). Integration of
54 lithospheric strain rates back through time implicates a ≥ 55 -km-thick crust within the TZ prior to
55 Miocene extension (Bahadori et al., 2018). Igneous geochemical studies are also consistent with
56 a previously thick TZ crust (~ 58 km at ~ 76 Ma; Chapman et al., 2020b). Garnet-clinopyroxenite
57 xenoliths in ~ 25 Ma TZ volcanic rocks (Fig. 1) are interpreted to represent cumulates or residues
58 that developed *in situ* during Laramide magmatism at depth (Erdman et al., 2016) or fragments
59 of the mafic keel to the Mojave batholith that were bulldozed beneath the TZ (Chapman et al.,
60 2020a; Rautela et al., 2020). Orocopia Schist exposed at Cemetery Ridge and the Plomosa
61 Mountains (Fig. 1; Jacobson et al., 2017; Seymour et al., 2018) would have abutted the
62 southwestern TZ prior to ~ 100 km of intervening Miocene northeast-southwest extension
63 (Spencer and Reynolds, 1989). If crustal thickening of the TZ by bulldozing did occur, it should
64 have been active at least when Orocopia Schist was being emplaced beneath western Arizona at
65 $\sim 70-65$ Ma (Chapman, 2016; Jacobson et al., 2017; Seymour et al., 2018), and might have
66 induced erosion-driven exhumation as topographic relief was generated in the TZ. This timing
67 prediction motivated our thermochronological study of the TZ.

68

69 PREVIOUS THERMOCHRONOLOGIC DATA

70 Thermochronological data record information about the timing of rock cooling below
71 their respective closure temperature windows, which are broad, but nominally ~250–400 °C for
72 biotite $^{40}\text{Ar}/^{39}\text{Ar}$, ~200–240 °C for zircon fission-track (ZFT), ~180 °C for zircon (U-Th-Sm)/He
73 (ZHe), ~60–115 °C for apatite fission-track (AFT), and ~60–80 °C for apatite (U-Th-Sm)/He
74 (AHe) (Reiners et al., 2018 and references therein). Biotite K-Ar and $^{40}\text{Ar}/^{39}\text{Ar}$ apparent ages
75 from Proterozoic TZ rocks are overwhelmingly Proterozoic (DeWitt et al., 2008 and references
76 therein). The Mesozoic – Cenozoic thermal history of the TZ is roughly constrained from three
77 AFT ± ZFT transects that span the Poachie, Bradshaw, and Mazatzal mountains (Fig. 2; Bryant
78 et al., 1991; Foster et al., 1993). These studies showed that TZ rocks cooled during Cretaceous –
79 Cenozoic time from temperatures of <120 °C near the Proterozoic unconformity to >200 °C at
80 the deeper structural levels now exposed in the southwest. The Poachie Mountains experienced
81 moderate rates of cooling between ~85 and 55 Ma (Bryant et al., 1991). Elsewhere in the TZ,
82 most AFT samples exhibit bimodal track-length distributions that suggest initial cooling during
83 the Laramide orogeny followed by ≤25 Ma cooling associated with extension (Foster et al.,
84 1993). There are no published ZHe or AHe data from the TZ, but an AHe investigation of the
85 southwestern-most margin of the Colorado Plateau suggests >1.5 km of Late Cretaceous
86 sedimentary burial followed by exhumation between ~60 and 50 Ma (Flowers et al., 2008).

87

88 METHODS

89 Our new igneous zircon U-Pb and biotite $^{40}\text{Ar}/^{39}\text{Ar}$, ZHe, AFT, and AHe data from the
90 ~northwest-trending Bradshaw Mountains come from samples of five Proterozoic granitoids, one

91 Late Cretaceous stock, and one modern river sand (Fig. 2) (see Supplemental Material for
92 analytical methods, data tables, supplementary data figures, and thermal modeling information).
93 The samples span a range-parallel distance of ~50 km and elevations ranging from 994 to 2212
94 m. To limit the effects of ≤ 25 Ma tectonic exhumation or sedimentary burial, we focused our
95 sampling within interior parts of the range located farthest away from Neogene extensional faults
96 and basins. The number of individual zircon crystals analyzed for each of the four ZHe samples
97 is only 2–4 because of their low yield of suitable zircons; for these samples we report their
98 unweighted mean age and standard deviation. A larger number of individual apatite crystals ($n =$
99 7–8) were analyzed for each of the three AHe samples; for these we report first quartile dates
100 (FQD), which have been shown to provide the most geologically meaningful information for
101 relatively low- n and relatively fast-cooled samples with dispersed single age distributions, along
102 with 1σ uncertainties quantified through non-parametric bootstrapping (He et al., 2021).

103

104 **RESULTS**

105 Proterozoic rocks in the Bradshaw Mountains are locally intruded by kilometer-scale
106 Late Cretaceous stocks with previously determined biotite/hornblende K-Ar dates ranging from
107 76 to 64 Ma (Fig. 2; DeWitt et al., 2008 and references therein). The K-Ar dates are generally
108 taken to approximate the timing of post-magmatic thermal equilibration, which occurs within a
109 few million years for stocks emplaced at shallow crustal depths (McInnes et al., 2005).

110 Supporting this assumption is the consistency between a newly determined U-Pb zircon mean
111 crystallization age of 71.9 ± 0.9 Ma (2σ ; $n = 33$ zircon laser spot ages; Fig. S1) for a tonalitic
112 stock (Sample A) and a biotite K-Ar date of ~70 Ma from an adjacent stock (Fig. 2). Sample A
113 yields single grain AHe dates ranging from ~37 to 66 Ma with a FQD of 44 ± 4 Ma (Fig. 3A),

114 suggesting that the stock remained at $T > \sim 60$ °C for >20 Myr after crystallization. Sample B of a
115 foliated Proterozoic granite located <1 km from a stock with a hornblende K-Ar date of ~ 64 Ma
116 yields a ZHe date of 66 ± 1 Ma ($n = 3$) (Figs. 2 and 3B). Sample C of a ~ 1.7 Ga granodiorite
117 located <1 km from a stock with a biotite K-Ar date of ~ 65 Ma yields an AFT central age of $61 \pm$
118 4 Ma and strongly dispersed individual AHe dates with a FQD of 52 ± 26 Ma (Figs. 2 and 3A).
119 Given their similarity to adjacent K-Ar dates, the ZHe and AFT dates from Samples B and C
120 likely reflect thermal perturbations associated with magmatism.

121 ZHe dates from northern-most Sample D and southern-most Sample E of Proterozoic
122 granitoids are 50 ± 4 Ma ($n = 3$) and 54.9 ± 0.5 Ma ($n = 2$), respectively (Figs. 2 and 3B). As
123 these ZHe dates are too young to reflect post-magmatic thermal equilibration, they are
124 interpreted to record cooling in response to erosion. Two $^{40}\text{Ar}/^{39}\text{Ar}$ incremental heating
125 experiments on biotite (one single-crystal, one 0.5 mg aliquot) from Sample E yield overall
126 similar and discordant age spectra that do not meet plateau criteria (Figs. S2 and S3). Apparent
127 ages increase from ~ 30 to ~ 50 Ma during progressive degassing and are younger than the two
128 individual ~ 55 Ma ZHe dates for the same sample. The most likely explanation for the
129 anomalously young apparent ages is partial alteration of biotite to vermiculate as determined
130 using Raman spectroscopy (Fig. S4).

131 Two $^{40}\text{Ar}/^{39}\text{Ar}$ incremental heating experiments on biotite (one single-crystal, one 1 mg
132 aliquot) from eastern-most Sample F of an ~ 1.7 Ga granite (DeWitt et al., 2008) yield similarly
133 shaped age spectra which range from ~ 0.8 Ga to ~ 1.4 Ga (Fig. S5). Omitting the initial $\sim 7\%$
134 $^{39}\text{Ar}_K$ from each experiment yields coeval inverse isochron ages of ~ 1.4 Ga with subatmospheric
135 $^{40}\text{Ar}/^{36}\text{Ar}$ intercept values resulting from apparent Ar loss (Fig. S6). Sample F also yields a ZHe
136 date of 64 ± 8 Ma ($n = 4$), an AFT central age of 53 ± 4 Ma, and an AHe FQD of 48 ± 8 Ma

137 (Figs. 2 and 3). Inverse thermal history modeling using QTQt 5.7.0 (Gallagher, 2012) on
138 Samples C and F (see Supplementary Material), integrating the AFT central age and single-
139 grain-age distribution, confined track-length distribution, thermal influence of the ~65 Ma stock
140 on Sample C, and ZHe and/or AHe single-grain dates, reveals an episode of accelerated cooling
141 (~10 °C/Myr) from ~150–200 °C to near-surface temperature between ~70 and 50 Ma (Fig. 3C).

142 Lastly, detrital AFT dates ($n = 117$) on Sample G of modern Hassayampa river sand yield
143 a unimodal distribution with a central age of 55.8 ± 1.4 Ma (Figs. 2 and S7). The catchment area
144 for Sample G is only ~9 km² but located ~20 km to the northwest of Sample F in a different
145 catchment with an indistinguishable AFT central age of 53 ± 4 Ma, suggestive of a similar and
146 regional low-temperature cooling history for the central Bradshaw Mountains.

147

148 **DISCUSSION AND CONCLUSIONS**

149 Our thermochronologic data from the Bradshaw Mountains suggest rapid (~10 °C/Ma)
150 cooling between ~70 and 50 Ma. Initial cooling at ~70–65 Ma could reflect post-magmatic
151 thermal equilibration, but most of the subsequent cooling is attributed to erosion. Both the
152 Poachie Mountains to the west and the southwestern-most Colorado Plateau to the northeast,
153 where Late Cretaceous intrusions are absent, experienced cooling between ~85–80 Ma and ~50
154 Ma (Bryant et al., 1991; Flowers et al., 2008; Fig. 3C). The Basin and Range province to the
155 southwest also records widespread ~80–50 Ma cooling prior to Miocene core complex
156 development (Fig. 2, e.g., Knapp and Heizler, 1990; Wong et al., 2023). The Orocopia Schist,
157 Maria fold-thrust belt, narrow northwest-trending belt of metamorphic core complexes between
158 Phoenix and southeastern California, garnet-clinopyroxenite xenolith localities, and the oldest
159 (Paleocene) Rim gravels in northwestern Arizona are all exposed along the trajectory where the

160 Farallon flat slab plowed into the southwest Cordilleran orogen (Fig. 1). We present a tentative
161 regional tectonic history that attempts to link these elements with the evolution of the TZ.

162 In contrast to the TZ, Late Cretaceous shortening is significant in southeastern California
163 and western Arizona as manifested by the basement-involved but thin-skinned-style and ductile
164 Maria fold-thrust belt (Fig. 1; Reynolds et al., 1986; Hamilton, 1987; Spencer and Reynolds,
165 1990; Boettcher et al., 2002). Thrusts and folds generally verge toward the south-southwest, in
166 contrast to the east-vergent Sevier thrust belt to the north (Fig. 1), and were active between ~90
167 and 70 Ma (Reynolds et al., 1986; Knapp and Heizler, 1990; Boettcher et al., 2002). Hence, the
168 Maria fold-thrust belt could have fed crust in the footwall of its decollement beneath the TZ (Fig.
169 4A). Underthrusting could explain ~85–70 Ma exhumation in the Poachie Mountains and thick
170 crust in the TZ by ~76 Ma (Chapman et al., 2020b).

171 The beginning of flat-slab subduction near the trench at ~90 Ma (Chapman, 2016) might
172 have accelerated shortening within the Maria fold-thrust belt, while the passage of the buoyant
173 flat slab and underplating of Orocochia Schist beneath the continental margin may have led to its
174 ~70–50 Ma extensional reactivation (e.g., Boettcher et al., 2002; Wong et al., 2023). ~70–50 Ma
175 cooling of the TZ, perhaps driven by inboard bulldozing of lithosphere beneath it, was coeval
176 with initial river incision and Rim gravel deposition in northwestern Arizona (Young and
177 Hartman, 2014; Hill et al., 2016) (Fig. 4B). Eclogite xenoliths in the Navajo Volcanic Field
178 suggest that the top of the Farallon slab was located at a depth of ~120 km beneath the Four
179 Corners region (Hernández-Urbe and Palin, 2019 and references therein), implicating a hinge in
180 the flat slab. A logical place for a hinge to form is where the flat slab first encountered stronger
181 lithosphere as it translated inboard. Lithosphere to the southwest of the TZ was weakened by
182 Mesozoic magmatism, lithospheric thinning during Border rift development, and Late

183 Cretaceous crustal shortening and anatexis (Jenney and Reynolds, 1989), whereas Colorado
184 Plateau lithosphere experienced none of this. The location of the hinge in the flat slab at the TZ
185 can also explain why bulldozed lithosphere thickened preferentially beneath it (Fig. 4B).
186 Beginning at ~25 Ma, ductile crust extruded to the southwest from beneath the TZ in the
187 footwalls of large-displacement detachment faults (Spencer and Reynolds, 1989; Bryant et al.,
188 1991), drainage reversed from northeastward to southwestward across the TZ (Anderson et al.,
189 2021; Potochnik et al., 2022), and volcanism became more widespread (Fig. 4C). Extensional
190 collapse is attributed to foundering of the Farallon slab and dense bulldozed lithosphere and was
191 directed southwestward by the buoyancy of the TZ crustal root (Fig. 4C; Chapman et al., 2020a).

192 **ACKNOWLEDGMENTS**

193 This research was supported by National Science Foundation (NSF) grant EAR-2048656. The
194 Arizona LaserChron Center and Noble Gas Laboratory are funded by NSF grants EAR-1649254
195 and -182692. We thank D. Alberts and J. Headley for laboratory assistance and A. Chapman, C.
196 Jacobson, and N. Seymour for constructive reviews.

197

198 **FIGURE CAPTIONS**

199 **Figure 1. Late Cretaceous – Eocene reconstruction of the American Southwest Cordillera**
200 **and major tectonic elements (modified after Chapman, 2016 and Saleeby, 2003). CR—**
201 **Cemetery Ridge, PI—Plomosa Mountains, X-Pz—nonconformity between Proterozoic**
202 **rocks and Paleozoic strata.**

203

204 **Figure 2. Shaded relief map (www.geomapapp.org) of west-central Arizona summarizing**
205 **previous and new (Samples A-G) thermochronologic results. Low-temperature**

206 **thermochronometric dates from the metamorphic core complexes (MCC) to the southwest**
207 **of the TZ are mostly Miocene while those in the hanging wall include older dates**
208 **overlapping with those from the TZ (e.g., Bryant et al., 1991; Foster et al., 1993; Singleton**
209 **et al., 2014; Prior et al., 2016).**

210

211 **Figure 3. A: Individual (black circles), median (black horizontal lines and lettering), and**
212 **first quartile apatite helium (AHe) dates (red horizontal lines and lettering); one >160 Ma**
213 **date from Sample C is excluded. B: ZHe (zircon helium) dates versus eU (effective uranium**
214 **concentration). C: Thermal history models performed in QTQt 5.7.0 (Gallagher, 2012) of**
215 **Samples C and F (blue lines with gray shading) and southwestern Colorado Plateau**
216 **samples CP-06-01, CP-06-19, and CP-06-20 of Flowers et al. (2008). Poachie Mountains**
217 **samples (Bryant et al., 1991) were not modeled because of insufficient single-grain data.**
218 **Thermal history modeling inputs and fits are provided in Supplementary Material. AHe**
219 **PRZ—apatite helium partial retention zone; AFT PAZ—apatite fission-track partial**
220 **annealing zone; ZHe PRZ—zircon helium partial retention zone.**

221

222 **Figure 4. Cross-sectional interpretations of the Late Cretaceous to Neogene tectonic**
223 **evolution of western Arizona. A: Maria fold-thrust belt shortening led to northeastward**
224 **underthrusting of crust beneath the TZ. MMT—Mule Mountains thrust. B: Flat-slab**
225 **oceanic subduction emplaced Orocopia Schist beneath western Arizona and bulldozed**
226 **continental lower crust and mantle lithosphere beneath the TZ. C: Foundering of Farallon**
227 **flat slab and dense bulldozed lithosphere resulted in volcanism, extensional collapse, and**
228 **drainage reversal across the TZ.**

229

230 **REFERENCES CITED**

- 231 Anderson, J. C., Karlstrom, K. E., and Heizler, M. T., 2021, Neogene drainage reversal and
232 Colorado Plateau uplift in the Salt River area, Arizona, USA: *Geomorphology*, v. 395,
233 <https://doi.org/10.1016/j.geomorph.2021.107964>.
- 234 Axen, G. J., van Wijk, J. W., and Currie, C. A., 2018, Basal continental mantle lithosphere
235 displaced by flat-slab subduction: *Nature Geoscience*, v. 11, p. 961-964,
236 <https://doi.org/10.1038/s41561-018-0263-9>.
- 237 Bahadori, A., Holt, W. E., and Rasbury, E. T., 2018, Reconstruction modeling of crustal
238 thickness and paleotopography of western North America since 36 Ma: *Geosphere*, v. 14,
239 p. 1207-1231, <https://doi.org/10.1130/GES01604.01601>.
- 240 Bird, P., 1984, Laramide crustal thickening event in the Rocky Mountain foreland and Great
241 Plains: *Tectonics*, v. 3, p. 741-758, <https://doi.org/10.1029/tc003i007p00741>.
- 242 Boettcher, S. S., Mosher, S., and Tosdal, R. M., 2002, Structural and tectonic evolution of
243 Mesozoic basement-involved fold nappes and thrust faults in the Dome Rock Mountains,
244 Arizona, in Barth, A., ed., *Contributions to Crustal Evolution of the Southwestern United*
245 *States*, Volume 365: Boulder, Geological Society of America Special Paper, p. 73-97,
246 <https://doi.org/10.1130/0-8137-2365-5.73>.
- 247 Bryant, B., Naeser, C. W., and Fryxell, J. E., 1991, Implications of low-temperature cooling
248 history on a transect across the Colorado Plateau-Basin and Range boundary, west central
249 Arizona: *Journal of Geophysical Research*, v. 96, p. 12375-12388,
250 <https://doi.org/10.1029/90jb02027>.

251 Chapman, A. D., 2016, The Pelona-Orocopia-Rand and related schists of southern California: a
252 review of the best-known archive of shallow subduction on the planet: *International*
253 *Geology Review*, p. 664-701, <https://doi.org/10.10180/00206814.00202016.01230836>.

254 Chapman, A. D., Rautela, O., Shields, J., Ducea, M. N., and Saleeby, J., 2020a, Fate of the lower
255 lithosphere during shallow-angle subduction: The Laramide example: *GSA Today*, v. 30,
256 p. 4-10, <https://doi.org/10.1130/GSATG1412A.1131>.

257 Chapman, J. B., Greig, R., and Haxel, G. B., 2020b, Geochemical evidence for an orogenic
258 plateau in the southern U.S. and northern Mexican Cordillera during the Laramide
259 orogeny: *Geology*, v. 48, p. 164-168, <https://doi.org/110.1130/G47117.47111>.

260 DeWitt, E., Langenheim, V., Force, E., Vance, R. K., Lindberg, P. A., and Driscoll, R. L., 2008,
261 *Geologic map of the Prescott National Forest and the headwaters of the Verde River,*
262 *Yavapai and Coconino counties, Arizona: U.S. Geological Survey Scientific*
263 *Investigations Map 2996, scale 1:100,000, 100 p. pamphlet,*
264 <https://doi.org/10.3133/sim2996>.

265 Erdman, M. E., Lee, C.-T. A., Levander, A., and Jiang, H., 2016, Role of arc magmatism and
266 lower crustal foundering in controlling elevation history of the Nevadaplano and
267 Colorado Plateau: A case study of pyroxenitic lower crust from central Arizona, USA:
268 *Earth and Planetary Science Letters*, v. 439, p. 48-57,
269 <https://doi.org/10.1016/j.epsl.2016.1001.1032>.

270 Flowers, R. M., Wernicke, B. P., and Farley, K. A., 2008, Unroofing, incision, and uplift history
271 of the southwestern Colorado Plateau from apatite (U-Th)/He thermochronometry:
272 *Geological Society of America Bulletin*, v. 120, p. 571-587,
273 <https://doi.org/10.1130/B26231.26231>.

274 Foster, D. A., Gleadow, A. J. W., Reynolds, S. J., and Fitzgerald, P. G., 1993, Denudation of
275 metamorphic core complexes and the reconstruction of the transition zone, west central
276 Arizona: Constraints from apatite fission track thermochronology: *Journal of*
277 *Geophysical Research*, v. 98, p. 2167-2185, <https://doi.org/10.1029/92JB02407>.

278 Gallagher, K., 2012, Transdimensional inverse thermal history modeling for quantitative
279 thermochronology: *Journal of Geophysical Research*, v. 117,
280 <https://doi.org/10.1029/2011JB008825>.

281 Hamilton, W., 1987, Mesozoic geology and tectonics of the Big Maria Mountains region,
282 southeastern California, in Dickinson, W. R., and Klute, M. A., eds., *Mesozoic rocks of*
283 *southern Arizona and adjacent areas*, Volume 18, *Arizona Geological Society Digest*, p.
284 33-47.

285 He, J., Thomson, S. N., Reiners, P. W., Hemming, S. R., and Licht, K. J., 2021, Rapid erosion of
286 the central Transantarctic Mountains at the Eocene-Oligocene transition: Evidence from
287 skewed (U-Th)/He date distributions near Beardmore Glacier: *Earth and Planetary*
288 *Science Letters*, v. 567, <https://doi.org/10.1016/j.epsl.2021.117009>.

289 Hernández-Uribe, D., and Palin, R. M., 2019, Catastrophic shear-removal of subcontinental
290 lithospheric mantle beneath the Colorado Plateau by the subducted Farallon slab:
291 *Scientific Reports*, v. 9, <https://doi.org/10.1038/s41598-41019-41446-41528-y>.

292 Hill, C.A., Polyak, V.J., Asmerom, Y., and Provencio, P.P., 2016, Constraints on a Late
293 Cretaceous uplift, denudation, and incision of the Grand Canyon region, southwestern
294 Colorado Plateau, USA, from U-Pb dating of lacustrine limestone: *Tectonics*, v.35, p.
295 896-906, <https://doi.org/10.1002/2016TC004166>.

296 Jacobson, C. E., Hourigan, J. K., Haxel, G. B., and Grove, M., 2017, Extreme latest Cretaceous-
297 Paleogene low-angle subduction: Zircon ages from Orocopia Schist at Cemetery Ridge,
298 southwestern Arizona, USA: *Geology*, v. 45, p. 951-954,
299 <https://doi.org/10.1130/G39278.1>.

300 Jenney, J. P., and Reynolds, S. J., eds., 1989, *Geologic Evolution of Arizona: Tucson, Arizona,*
301 *Arizona Geological Society Digest 17*, 866 p.

302 Knapp, J. H., and Heizler, M. T., 1990, Thermal history of crystalline nappes of the Maria fold
303 and thrust belt, west central Arizona: *Journal of Geophysical Research*, v. 95, p. 20049-
304 20073, <https://doi.org/10.1029/JB095ib12p20049>.

305 Livaccari, R. F., Burke, K., and Sengor, A. M. C., 1981, Was the Laramide orogeny related to
306 subduction of an oceanic plateau?: *Nature*, v. 289, p. 276-278,
307 <https://doi.org/10.1038/289276a0>.

308 McInnes, B. I. A., Evans, N. J., Fu, F. Q., and Garvin, S., 2005, Application of
309 thermochronology to hydrothermal ore deposits: *Review in Mineralogy and*
310 *Geochemistry*, v. 58, p. 467-498, <https://doi.org/10.2138/rmg.2005.58.18>.

311 Potochnik, A. R., Faulds, J. E., and Reynolds, S. R., 2022, Cenozoic drainage reversal on the
312 southern margin of the Colorado Plateau, east-central Arizona, USA: *Geomorphology*, v.
313 411, <https://doi.org/10.1016/j.geomorph.2022.108286>.

314 Prior, M.G., Stockli, D.F., and Singleton, J.S., 2016, Miocene slip history of the Eagle Eye
315 detachment fault, Harquahala Mountains metamorphic core complex, west-central
316 Arizona: *Tectonics*, v. 35, p. 1913-1934, <https://doi.org/10.1002/2016TC004241>.

317 Qashqai, M. T., Afonso, J. C., and Yang, Y., 2016, The crustal structure of the Arizona
318 Transition Zone and southern Colorado Plateau from multiobservable probabilistic

319 inversion: *Geochemistry, Geophysics, Geosystems*, v. 17, p. 4308-4332,
320 <https://doi.org/10.1002/2016GC006463>.

321 Rautela, O., Chapman, A. D., Shields, J. E., Ducea, M. N., Lee, C.-T., Jiang, H., and Saleeby, J.,
322 2020, In search for the missing arc root of the Southern California Batholith: P-T-t
323 evolution of upper mantle xenoliths of the Colorado Plateau Transition Zone: *Earth and*
324 *Planetary Science Letters*, v. 547, <https://doi.org/10.1016/j.epsl.2020.116447>.

325 Reiners, P. W., Carlson, R. W., Renne, P. R., Cooper, K. M., Granger, D. E., McLean, N. M.,
326 and Schoene, B., 2018, *Geochronology and Thermochronology*, Oxford, John Wiley and
327 Sons Ltd, 464 p.

328 Reynolds, S. J., Spencer, J. E., Richard, S. M., and Laubach, S. E., 1986, Mesozoic structures in
329 west-central Arizona, in Beatty, B., and Wilkinson, P. A., eds., *Frontiers in Geology and*
330 *Ore Deposits of Arizona and the Southwest*, Arizona Geological Society Digest Volume
331 16, p. 35-51.

332 Saleeby, J., 2003, Segmentation of the Laramide Slab—evidence from the southern Sierra Nevada
333 region: *Geological Society of America Bulletin*, v. 115, p. 655-668,
334 [https://doi.org/10.1130/0016-7606\(2003\)115<0655:SOTLSF>2.0.CO;2](https://doi.org/10.1130/0016-7606(2003)115<0655:SOTLSF>2.0.CO;2).

335 Seymour, N. M., Strickland, E. D., Singleton, J. S., Stockli, D. F., and Wong, M. S., 2018,
336 Laramide subduction and metamorphism of the Orocopia Schist, northern Plomosa
337 Mountains, west-central Arizona: Insights from zircon U-Pb geochronology: *Geology*, v.
338 46, p. 847-850, <https://doi.org/10.1130/G45059.45051>.

339 Singleton, J.S., Stockli, D.F., Gans, P.B., and Prior, M.G., 2014, Timing, rate, and magnitude of
340 slip on the Buckskin-Rawhide detachment fault, west central Arizona: *Tectonics*, v. 33, p.
341 1596-1615, <https://doi.org/10.1002/2013TC003517>.

342 Spencer, J. E., and Reynolds, S. J., 1990, Relationship between Mesozoic and Cenozoic tectonic
343 features in west central Arizona and adjacent southeastern California: Journal of
344 Geophysical Research, v. 95, p. 539-555, <https://doi.org/10.1029/JB095ib01p00539>.

345 Wong, M.S., Singleton, J.S., Seymour, N.M., Gans, P.B., and Wrobel, A.J., 2023, Late
346 Cretaceous-early Paleogene extensional ancestry of the Harcuvar and Buckskin-Rawhide
347 metamorphic core complexes, western Arizona: Tectonics, v. 42, e2022TC007656,
348 <https://doi.org/10.1029/2022TC007656>.

349 Young, R. A., and Hartman, J. H., 2014, Paleogene rim gravel of Arizona: Age and significance
350 of the Music Mountain Formation: Geosphere, v. 10, p. 870-891,
351 <https://doi.org/10.1130/GES00971.00971>.

352

353 ¹Supplemental Material. [*Analytical methods, data tables and figures, and thermal modeling*
354 *information.*] Please visit <https://doi.org/10.1130/XXXX> to access the supplemental material,
355 and contact editing@geosociety.org with any questions.

Figure 1 Kapp et al.

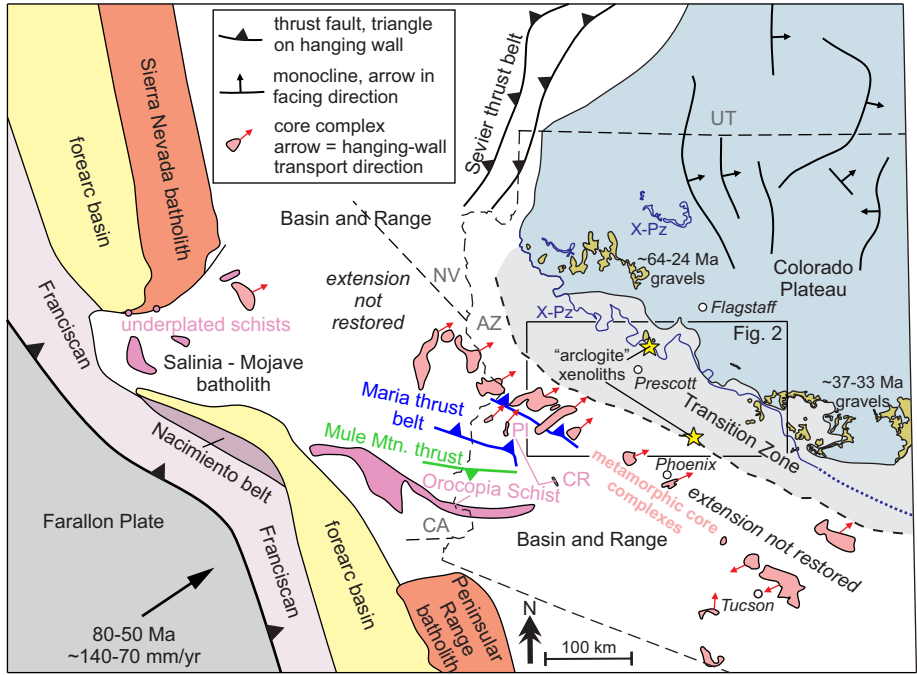


Figure 2 Kapp et al.

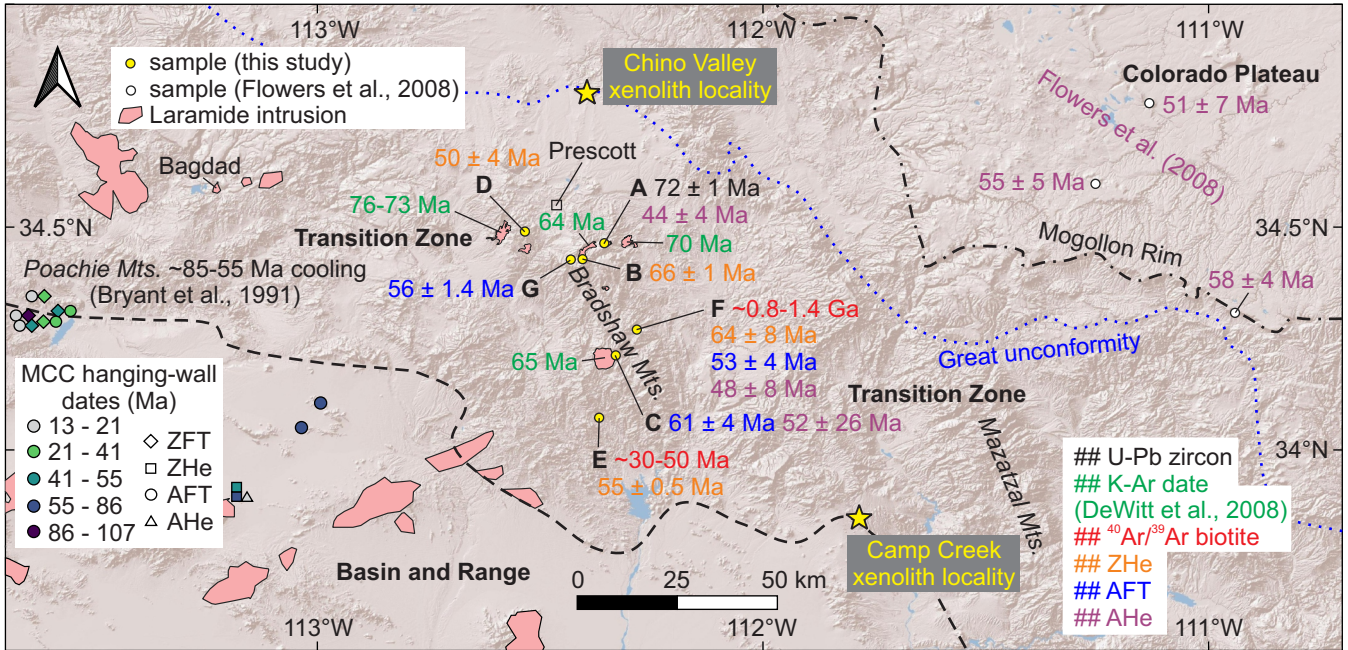


Figure 3 Kapp et al.

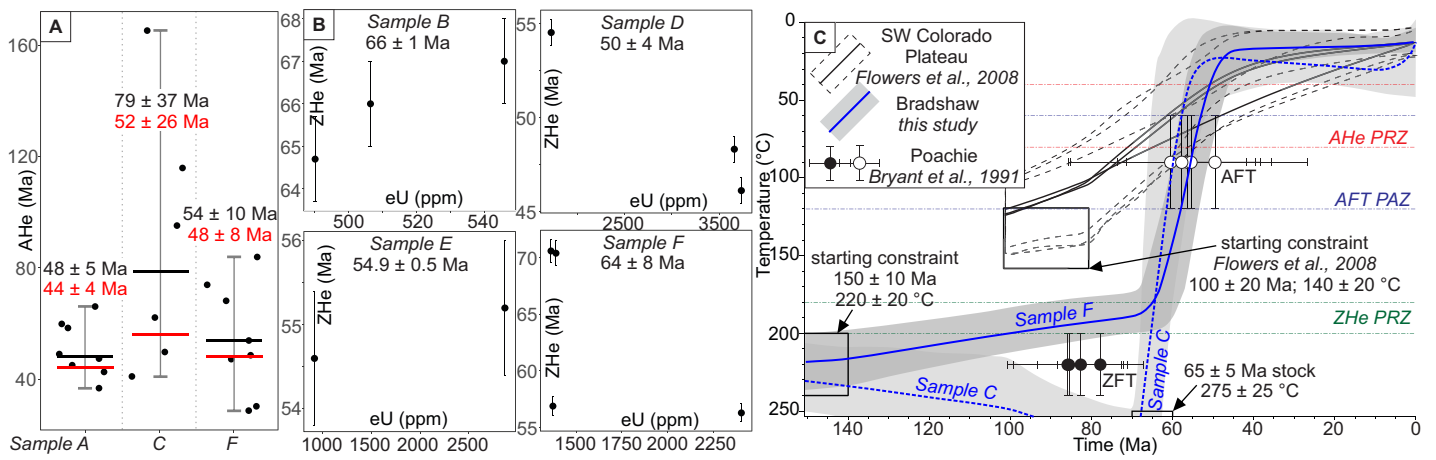
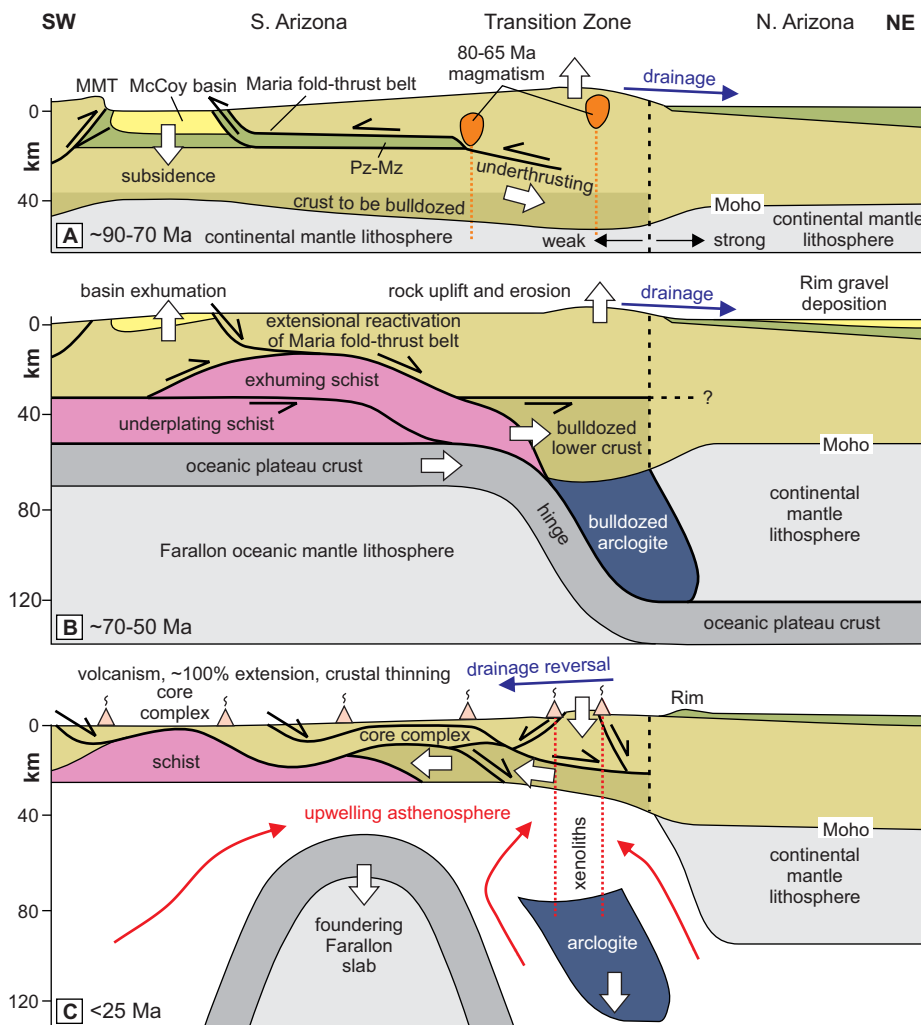


Figure 4 Kapp et al.



Zircon U-Pb LA-ICP-MS Methodology

Sample A (manuscript name; 9.8.20.2PK is primary sample name) was analyzed following standard procedures for zircon U-Pb geochronology by LA-ICP-MS at the Arizona Laserchron Center (ALC; www.laserchron.org; Gehrels et al., 2008, Gehrels and Pecha, 2014).

Zircon Separation, Mount Preparation, and Data Acquisition

Zircons were separated from ~1 kg of rock using traditional methods of crushing, water separation, magnetic separation, and heavy liquids separation (Gehrels et al., 2008). Grains were picked and mounted in epoxy with primary reference material FC-1 (isotope dilution-thermal ionization mass spectrometry [ID-TIMS] age of 1099.0 ± 0.6 Ma), secondary reference material SL-F (ID-TIMS age of 555.86 ± 0.68 Ma), and tertiary reference material R33 (ID-TIMS age of 419.3 ± 0.4 Ma) (Paces and Miller, 1993; Black et al., 2004; S. Bowring, 2017, personal communication with George Gehrels regarding unpublished report titled “MIT LA SRI LAN F” that details the ID-TIMS age for a natural reference material). The epoxied mount was polished to maximize the exposed surface area of zircon and back-scattered electron images were produced using a Hitachi 3400N scanning electron microscope as reference images for laser spot placement prior to data acquisition.

Igneous zircon U-Pb analysis by LA-ICP-MS was conducted at the ALC following the methods of Gehrels et al. (2008), Gehrels and Pecha (2014), and Pullen et al. (2018).

Instrumentation consisted of Photon Machines Analyte-G2 ArF 193 nm excimer laser with a HelEx2 ablation cell connected to a Thermo Element2 high-resolution single-collector ICP-MS via an aerosol rapid introduction system. In total, 35 unknowns, 18 primary reference materials (FC-1), 9 secondary reference materials (SL-F), and 5 tertiary reference materials (R33) were

analyzed using sample-standard bracketing to monitor instrument drift over the data acquisition session by checking for systematic shifts in ages of the reference materials relative to their accepted ID-TIMS values. Prior to the first analysis, all laser spots were ablated with a 50 μm cleaning shot to remove common Pb and/or surface contaminants. Each spot was then analyzed using a 30 μm laser spot and ablated to a depth of ~ 15 μm . Ablated material was carried by helium gas into the plasma source of the mass spectrometer and isotopes of U, Th, Pb, and Hg were detected via dual mode secondary electron multiplier and analyzed in sequence via peak-hopping.

Data Reduction

Isotopic data were reduced at the ALC using the in-house *Excel*-based program *E2agecalc*. Before raw data are converted to isotopic ratios of interest ($^{206}\text{Pb}/^{238}\text{U}$, $^{206}\text{Pb}/^{207}\text{Pb}$, and $^{208}\text{Pb}/^{232}\text{Th}$), ion intensities of individual isotopes are first corrected by subtracting backgrounds, accounting for isobaric interferences, and correcting for common Pb (Stacey and Kramers, 1975). The preliminary isotopic ratios from analyses of primary reference materials are then compared to accepted values to determine fractionation factors for $^{206}\text{Pb}/^{238}\text{U}$, $^{206}\text{Pb}/^{207}\text{Pb}$, and $^{208}\text{Pb}/^{232}\text{Th}$, and the fractionation factor is applied to all analyses using a sliding-window average. Uncertainties are then propagated following the methods of Gehrels et al. (2008) and Gehrels and Pecha (2014).

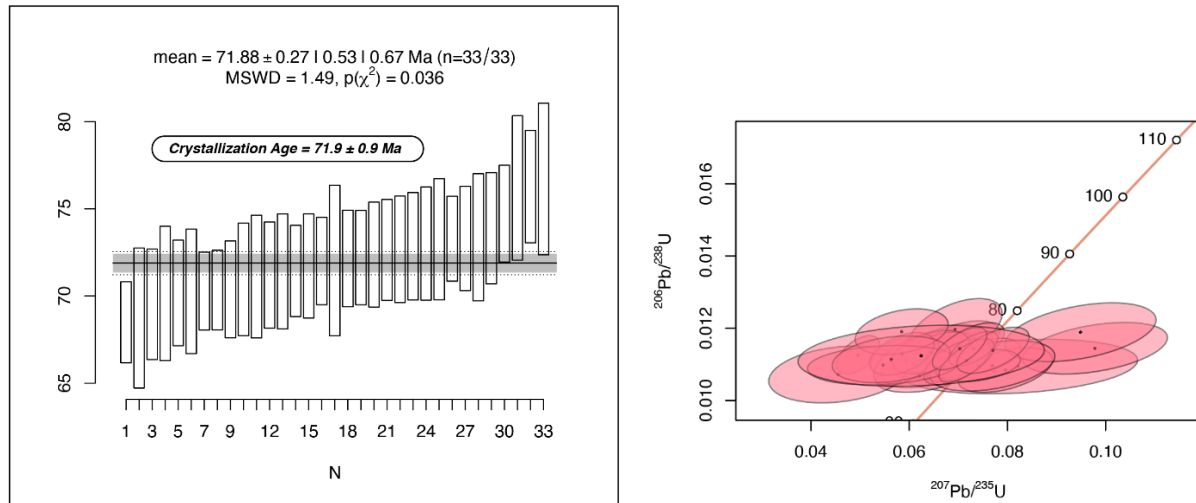


Figure S1. Weighted mean age and Concordia plots for Sample A. The large uncertainties in the $^{207}\text{Pb}/^{238}\text{U}$ measurements are because of low U concentrations (generally <75 ppm) and the relatively young age of the sample, which leads to large uncertainties in measuring ^{207}Pb and the common Pb correction.

$^{40}\text{Ar}/^{39}\text{Ar}$ thermochronology methods

Four $^{40}\text{Ar}/^{39}\text{Ar}$ incremental heating experiments were conducted on biotite from two Proterozoic granite samples in the Arizona Transition Zone (Bradshaw Mountains) at the Arizona Noble Gas Laboratory at the University of Arizona. Mineral separates were isolated from the rocks by crushing, sieving from 350 to 500 μm , and then hand-picked under a binocular microscope to isolate single grains. The purified separates were wrapped in aluminum foil, placed in 2.5 cm aluminum disks, and irradiated along with the 28.201 Ma Fish Canyon sanidine standard (Kuiper et al., 2008) at the Oregon State University TRIGA reactor in the Cadmium-Lined In-Core Irradiation Tube (CLICIT). Aliquots (0.5-1 mg) and single crystals of biotite were placed in a 5 mm well within a copper planchette and incrementally heated with a Teledyne Instruments 55 W CO_2 laser. Extracted gas was cleaned for 20-30 mins using two SAES GP50

getter at 450°C, one SAES NP10 getter at room temperature, and an Edwards Polycold® PCC Compact Cooler maintained at -90 °C before being analyzed using a Thermo Fisher Scientific Argus VI multicollector noble gas mass spectrometer. $^{40}\text{Ar}/^{39}\text{Ar}$ dates are calculated using the decay constants of Min et al. (2000) and analytical uncertainties, including J contributions, are reported at 2σ . Samples were corrected using an atmospheric $^{40}\text{Ar}/^{36}\text{Ar}$ ratio of 298.56 ± 0.31 (Lee et al., 2006). Data reduction was performed using Pychron software (Ross, 2019).

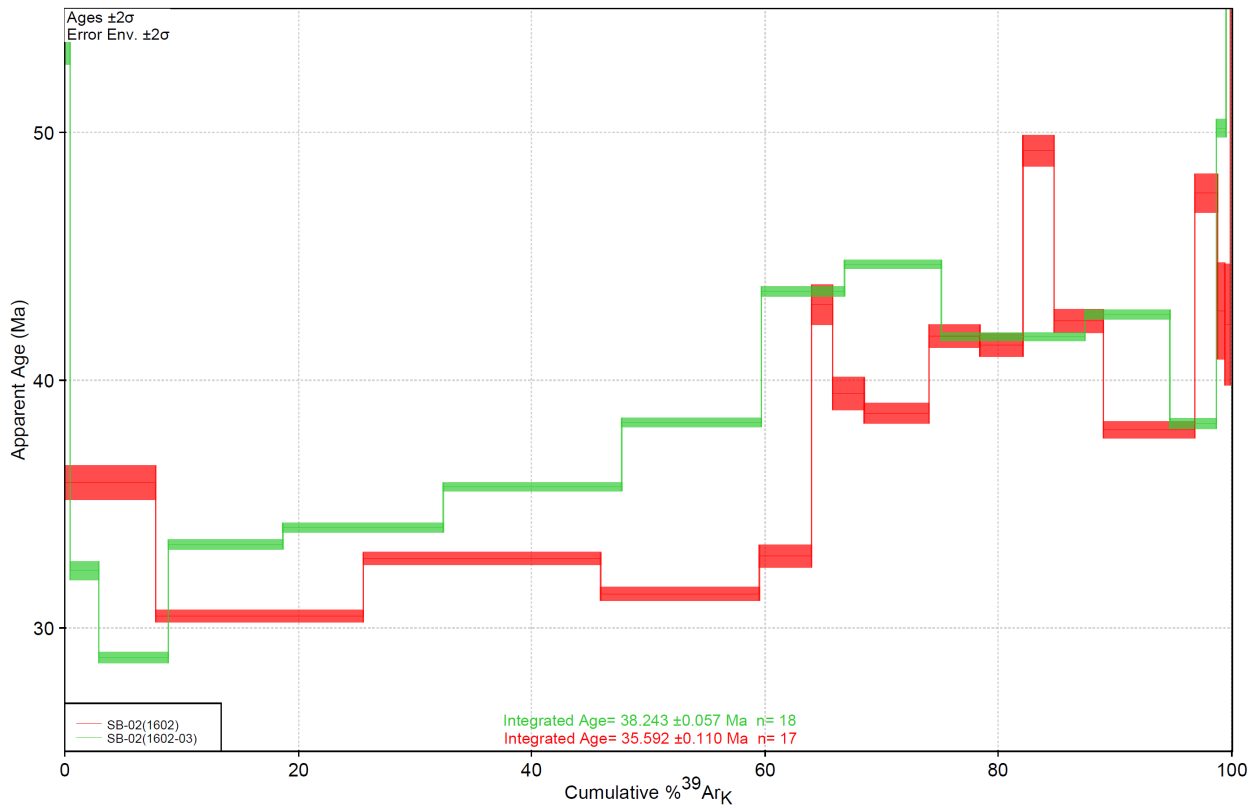


Figure S2. Biotite $^{40}\text{Ar}/^{39}\text{Ar}$ apparent age spectra for one single-crystal and one 0.5 mg aliquot from manuscript Sample E (original sample name SB-02).

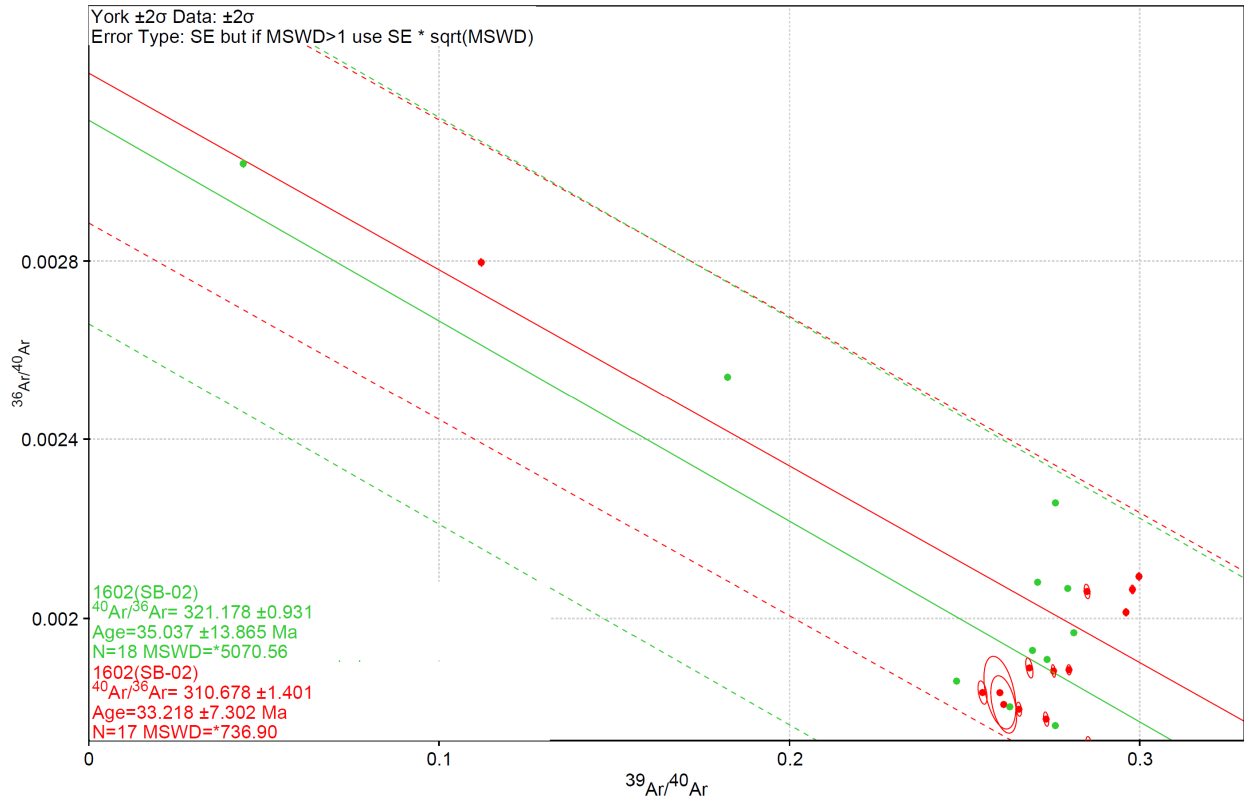


Figure S3. Inverse isochron plots for manuscript Sample E (original Sample SB-02). Low ^{36}Ar abundances preclude calculation of well-defined isochrons with little spread in $^{36}\text{Ar}/^{40}\text{Ar}$.

$^{40}\text{Ar}/^{36}\text{Ar}$ intercepts (311, 320) are in excess of modern atmosphere ($^{40}\text{Ar}/^{36}\text{Ar} = 298.56$, Lee et al., 2006) although given the poorly defined isochrons the presence of excess Ar in this sample is questionable.

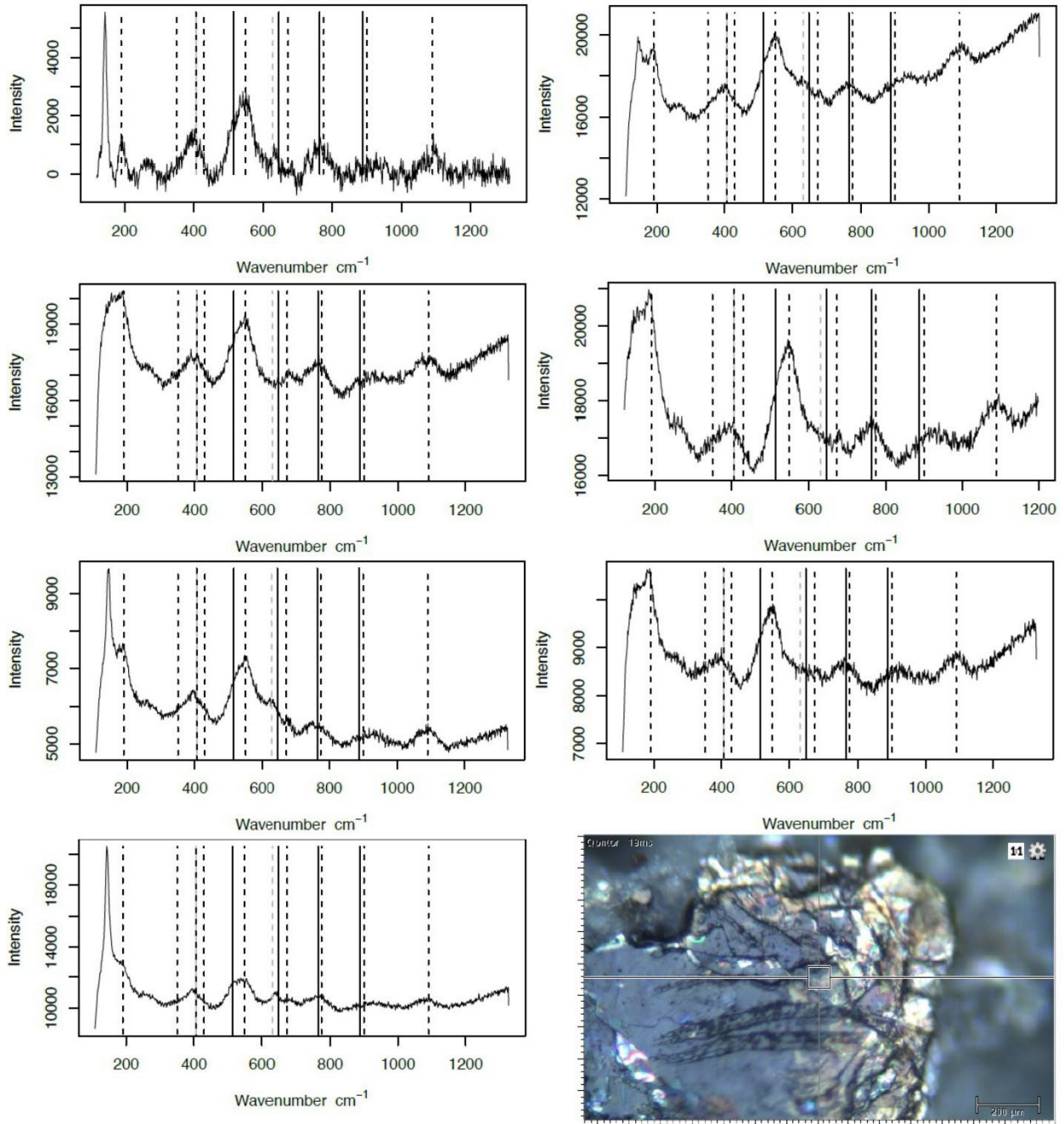


Figure S4. Raman spectroscopy results for biotite from Sample E (original Sample SB-02). The spectra show signs of alteration from pure biotite (peaks corresponding to solid lines; Dumańska-Slowik et al., 2015) to vermiculite (peaks corresponding to dashed lines; Wang et al., 2015; Ritz and Valášková, 2018). Lower right is a representative reflected light image.

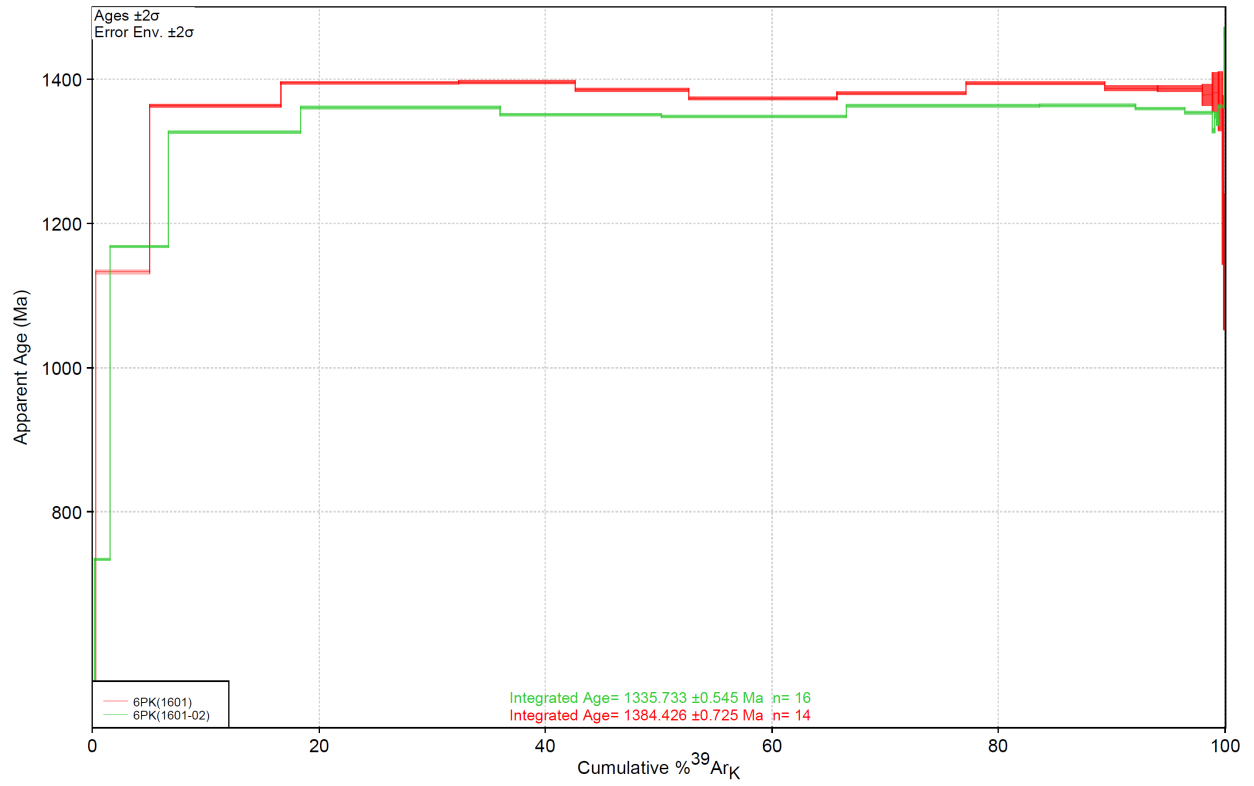


Figure S5. Biotite $^{40}\text{Ar}/^{39}\text{Ar}$ apparent age spectra for one single-crystal and one 1 mg aliquot from manuscript Sample F (original sample name 10.10.20.6PK).

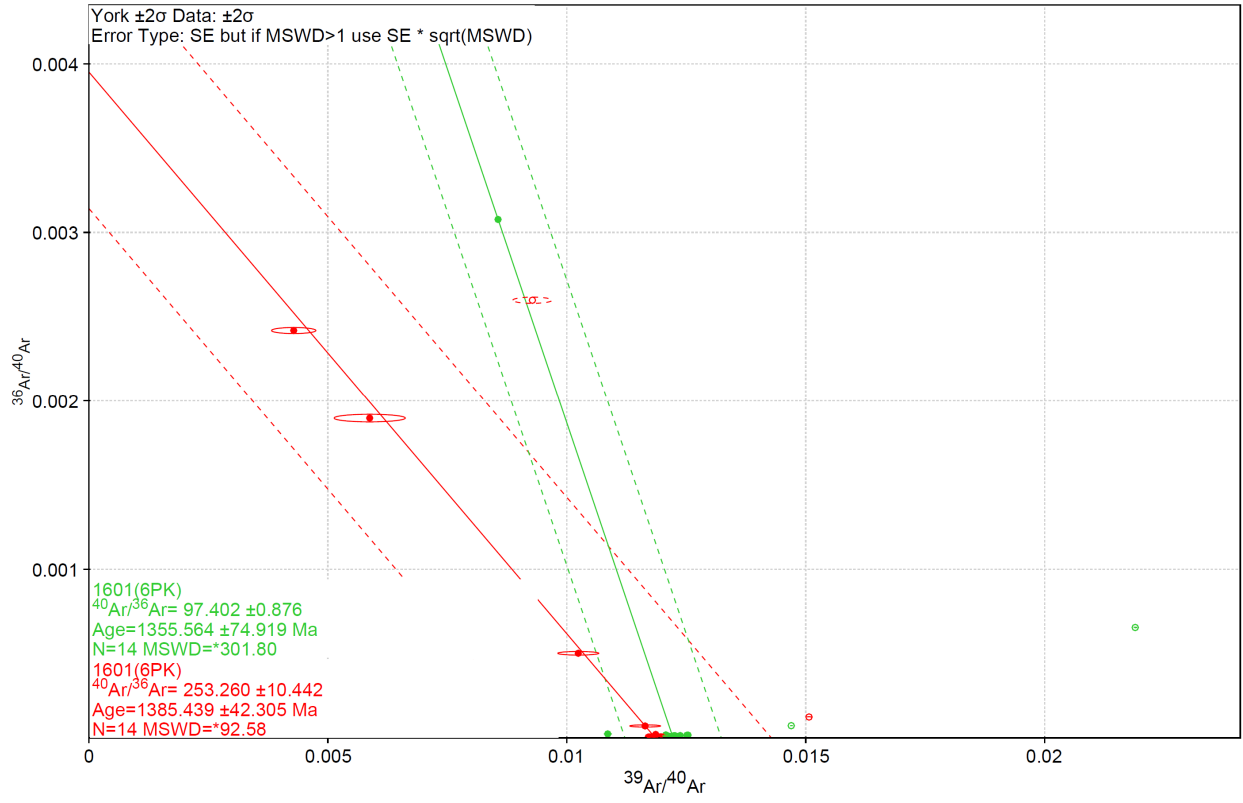


Figure S6. Inverse isochron plots for manuscript Sample F (original sample name 10.10.20.6PK).

Apatite fission-track methods

The fission-track thermochronometer relies on the spontaneous fission decay of ^{238}U (Hurford and Green, 1983). Spontaneous fission within apatite is annealed between temperatures of $\sim 120\text{--}60\text{ }^\circ\text{C}$, making this system useful for constraining upper-crustal cooling (e.g., Braun et al., 2006, and references within). The fission-track analyses were performed at the University of Arizona Fission Track Laboratory. Apatites were extracted via standard heavy mineral techniques. Apatite crystals are mounted in epoxy and polished to reveal their internal sections, with spontaneous fission-tracks revealed through etching with 5.5 M nitric acid for 20 s at 21 $^\circ\text{C}$ before irradiation (after Donelick et al., 2005). Samples were analyzed via the external detector method (Gleadow et al., 1976) which utilizes low uranium muscovite mica detectors, and were

irradiated at the Oregon State University Triga Reactor, Corvallis, USA. The total neutron fluence was checked using CN5 U-doped. Following irradiation, the mica sheets were etched in 40% hydrofluoric acid for 45 min at 21 °C (after Donelick et al., 2005). Apatite fission-tracks were counted using an Olympus BX51 microscope with an associated digitizing tablet and computer controlled stage (Kinetek) in Tucson at x1600 magnification. Confined fission-track length distributions were obtained to determine cooling rates; mean track lengths (MTLs) of $>13.5 \mu\text{m}$ are considered to be reflective of rapid cooling (Ketcham et al., 2007). The central ages were calculated by using the ζ -method after Hurford and Green (1983) (Table 2). Radial plots were produced using radial plotter (Vermeesch, 2009). Apatite fission-track ages were calculated using a ζ -value of 341.6 ± 8.5 (GJ).

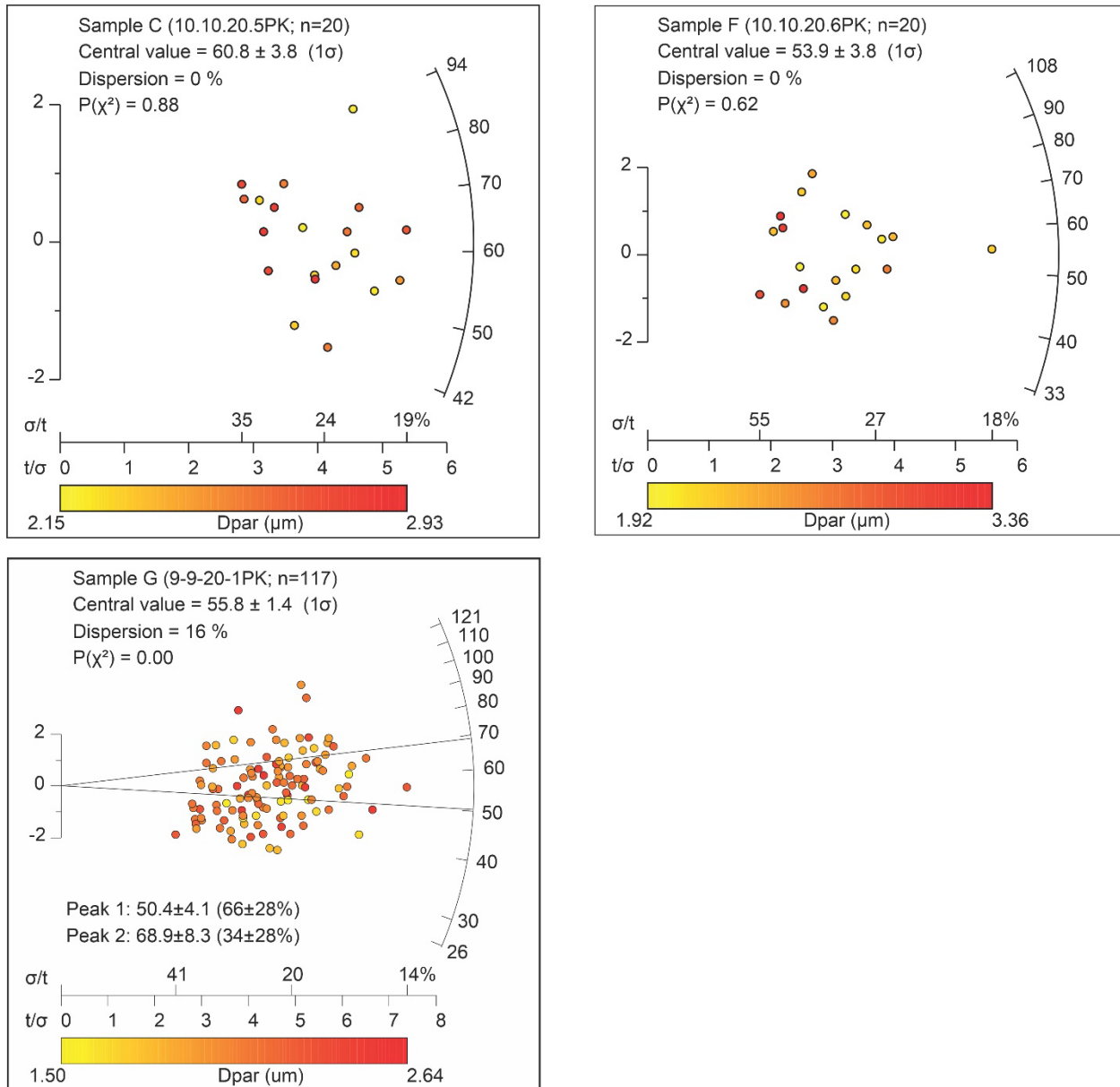


Figure S7. Radial fission-track plots for Samples C, F, and G.

Zircon and apatite (U-Th-[Sm])/He methods

All (U-Th)/He analyses were performed at the University of Arizona Noble Gas Laboratory. Apatite and zircon crystals were extracted from crushed samples following routine mineral separation protocols, and individually reviewed for inclusions, imperfections, fractures, coatings, and fragmentation. Crystals were photographed and measured under a high-powered

stereo-zoom microscope on two sides. They were then packed individually in Nb envelopes and degassed by laser heating up to ~900-1300 °C, with higher temperature used for zircon degassing. Reference Durango standards were analyzed at the beginning, middle, and end of each analysis run along with unknowns to account for variation in isotopic fractionation or sensitivity bias. ⁴He was measured by isotope dilution with a quadrupole mass spectrometer. Nb envelopes and included apatite/zircon crystals were then transferred to Teflon vials and dissolved. U-Th-Sm (plus Ca in apatite and Zr in zircon) were measured by isotope dilution on a high-resolution single-collector sector ICP-MS. We applied corrections to account for alpha-ejection using measurements of crystal dimension (assuming hexagonal prism geometry, for apatite, and orthorhombic prism with pyramidal terminations, for zircons) (Farley, 2002), with updated alpha-ejection correction calculations for fragmented grains (He and Reiners, 2022). Detailed procedures can be found in Reiners et al. (2018), or lab protocols posted on the University of Arizona helium laboratory website (<https://www.geo.arizona.edu/~reiners/arhdl/methodsalready.pdf>), with the exception of the updated fragmentation correction referenced above (He and Reiners, 2022).

We report all single-aliquot analyses in supplementary Table S4, and note in red any anomalous data that were not included in the calculation of summary statistics for any given sample. Because samples yielded few zircon grains, no zircon analyses were excluded from consideration. We also report the mean, median, and for apatite helium analyses, the first quartile date (FQD) for each sample (He et al., 2021), the latter to account for the far higher likelihood of errors that skew corrected dates to be many multiples older (in particular, the effect of helium implantation from adjacent high-eU accessory minerals like zircon into low-eU apatite crystals, i.e. “parentless” helium) than errors that skew dates to be younger in apatite helium samples

(Spiegel et al., 2009; Gautheron et al., 2012; He et al., 2021; Flowers et al., 2023). Uncertainties (1σ) were calculated using non-parametric bootstrapping (with resampling, $n = 10000$), which has the advantage of avoiding the assumption that the underlying distribution is distributed normally (He et al., 2021).

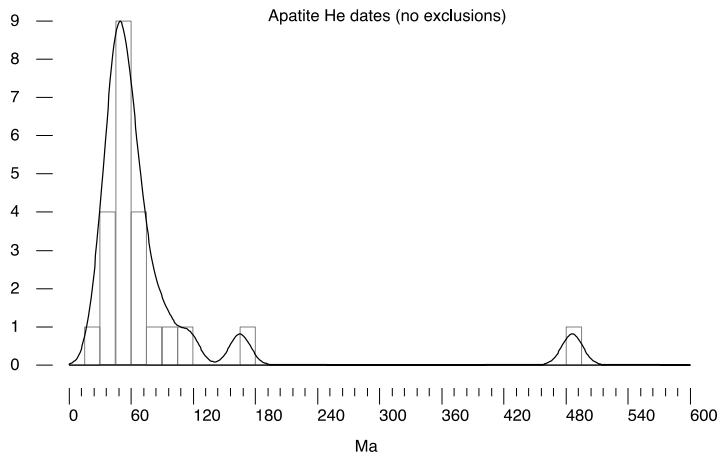
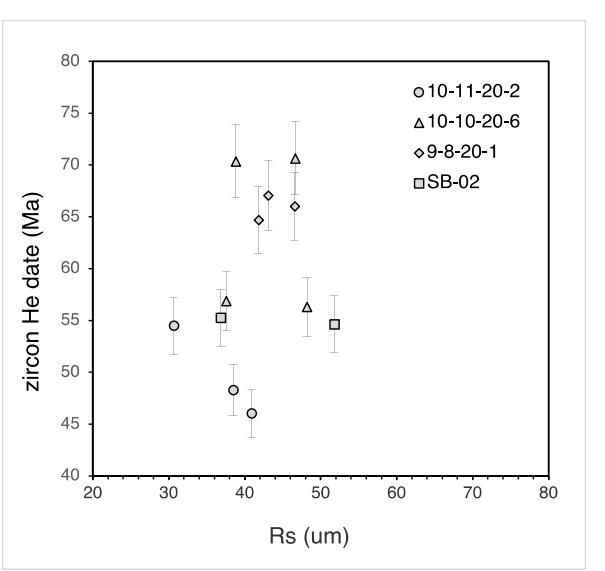
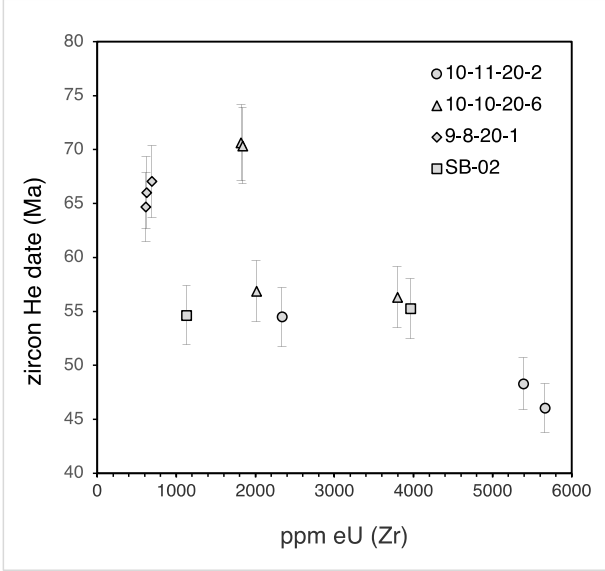
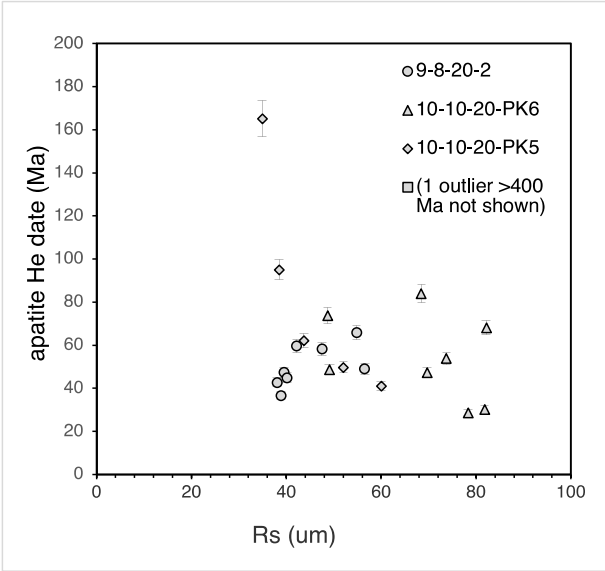
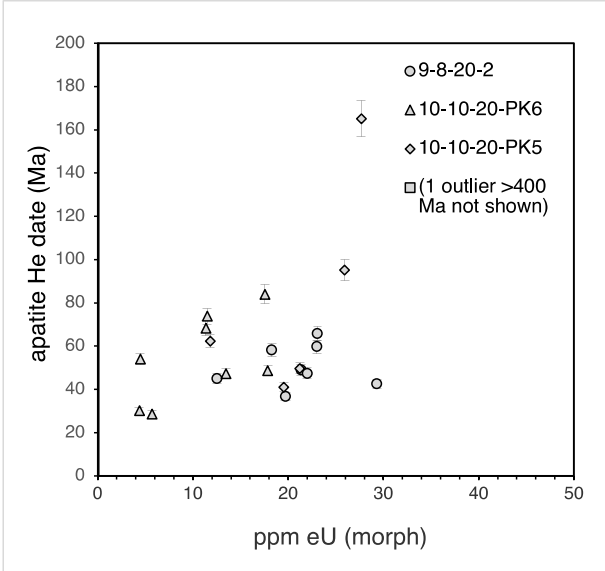


Figure S8. Supplementary apatite and zircon helium figures. eU – effective uranium concentration; R_s – sphere-equivalent radius.

Thermal history modeling:

Inverse thermal history modeling using QTQt 5.7.0 (Gallagher, 2012) was conducted on manuscript Sample C and Sample F in the Bradshaw Mountains and previously published apatite (U-Th-Sm)/He data from three samples analyzed along the southern margin of the Colorado Plateau (CP-0501, CP-06-19, CP-06-20; Flowers et al., 2008). The QTQt software applies a Bayesian trans-dimensional approach to Markov Chain Monte Carlo statistics (Gallagher 2012) to produce a cooling evolution of the sample that predicts the measured data by applying the AFT annealing model after Ketcham et al. (2007) and the AHe diffusion model after Flowers et al. (2009). Our approach used an initial unconstrained run to explore the statistical space, that was then followed by adjustments to the search parameters as well as the addition of geological constraints. A large number of iterations ($n \gg 100,000$) were run to generate a range of models that can constrain a probability distribution. From the obtained probability distribution an individual thermal history can be selected, such as the maximum likelihood as well as an “expected” (weighted mean) paths. We followed acceptance rates for models that were between 0.1 and 0.6 and with a birth-death ratio of ~ 1 . Model input data, assumptions, uncertainties, and other system- and model-specific parameters are provided in Table S6 following the framework established by Flowers et al. (2015).

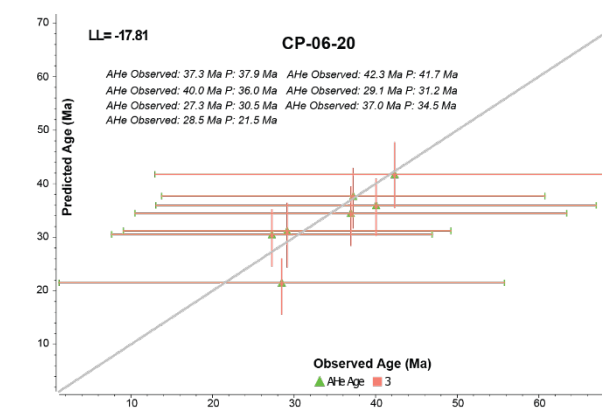
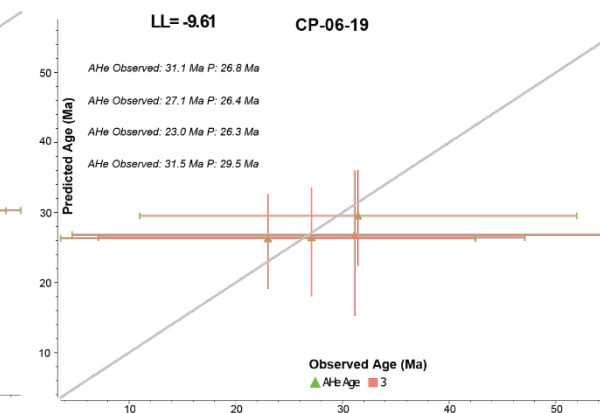
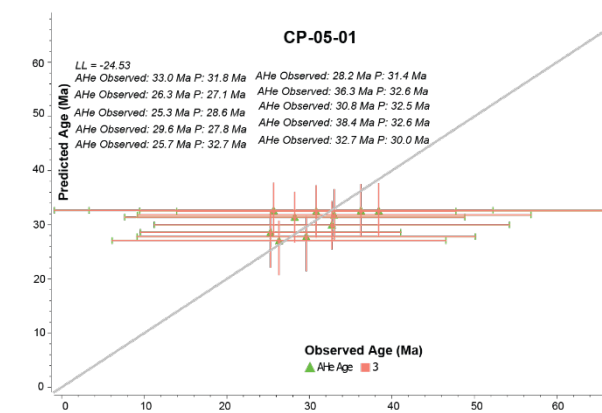
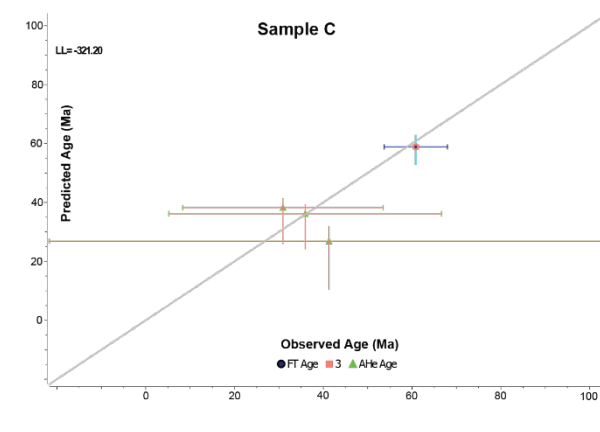
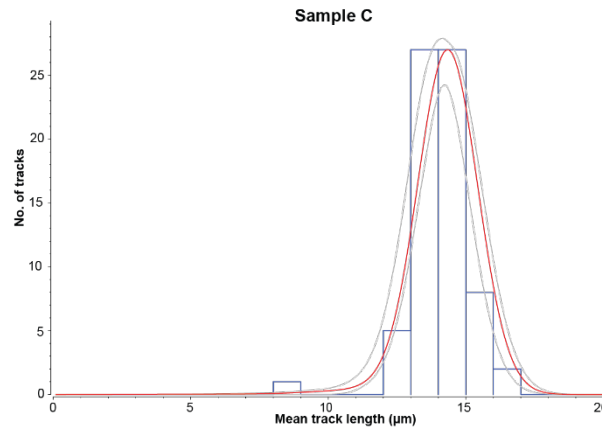
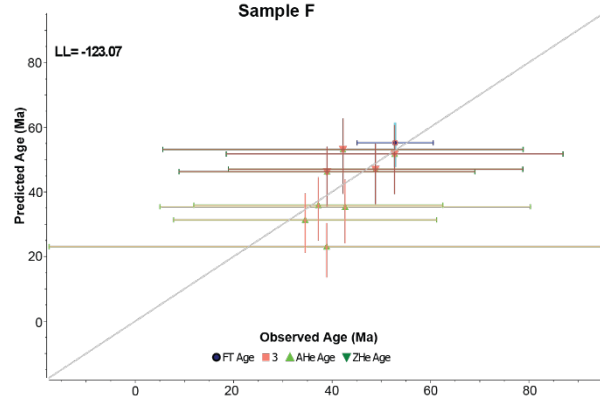
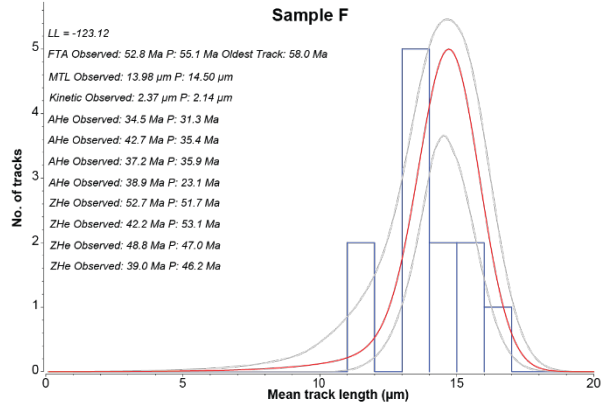


Figure S9. Predicted versus observed for thermal history modeling of Samples C and F (this study) and those of Flowers et al., 2008. AHe – apatite (U-Th-Sm)/He; FTA – fission-track analysis; MTL – mean track length; LL – log-likelihood; Kinetic is Dpar.

REFERENCES CITED

- Black, L.P., Kamo, S.L., Allen, C.M., Davis, D.W., Aleinikoff, J.N., Valley, J.W., Mundil, R., Campbell, I.H., Korsch, R.J., and Williams, I.S., 2004, Improved $^{206}\text{Pb}/^{238}\text{U}$ microprobe geochronology by the monitoring of a trace-element-related matrix effect; SHRIMP, ID-TIMS, ELA-ICP-MS and oxygen isotope documentation for a series of zircon standards: *Chemical Geology*, v. 205, p. 115-140.
- Braun, J., van der Beek, P., and Batt, G., 2006, *Quantitative thermochronology: Numerical methods for the interpretation of thermochronological data*: Cambridge University Press, 272 p.
- Donelick, R.A., O'Sullivan, P.B., and Ketcham, R.A., 2005, Apatite fission-track analysis: *Reviews in Mineralogy and Geochemistry*, v. 58, p. 49-94,
<https://doi.org/10.2138/rmg.2005.58.3>.
- Dumańska-Słowik, M., Weselucha-Birczyńska, A., and Pieczka, A., 2015, Micas from mariupolite of the Oktiabrski massif (SE Ukraine): An insight into the host rock evolution – Geochemical data supported by Raman microspectroscopy: *Spectrochimica Acta Part A: Molecular and Biomolecular Spectroscopy*, v. 137, p. 817-826,
<https://doi.org/10.1016/j.saa.2014.08.127>.
- Farley, K.A., 2002, (U-Th)/He dating: techniques, calibrations, and applications: *Reviews of Mineralogy and Geochemistry*, v. 47, p. 819–844,
<https://doi.org/10.2138/rmg.2002.47.18>.

- Flowers, R.M., Farley, K.A., and Ketcham, R.A., 2015, A reporting protocol for thermochronologic modeling illustrated with data from the Grand Canyon: Earth and Planetary Science Letters, v. 432, p. 425-435, <https://doi.org/10.1016/j.epsl.2015.09.053>.
- Flowers, R.M., Ketcham, R.A., Enkelmann, E., Gautheron, C., Reiners, P.W., Metcalf, J.R., Danišik, M., Stockli, D.F., and Brown, R. W., 2023, (U-Th)/He chronology: Part 2. Considerations for evaluating, integrating, and interpreting conventional individual aliquot data: GSA Bulletin, v. 135, p. 137-161, <https://doi.org/10.1130/B36268.1>.
- Flowers, R. M., Wernicke, B. P., and Farley, K. A., 2008, Unroofing, incision, and uplift history of the southwestern Colorado Plateau from apatite (U-Th)/He thermochronometry: Geological Society of America Bulletin, v. 120, p. 571-587, <https://doi.org/10.1130/B26231.26231>.
- Gallagher, K., 2012, Transdimensional inverse thermal history modeling for quantitative thermochronology: Journal of Geophysical Research, v. 117, <https://doi.org/10.1029/2011JB008825>.
- Gautheron, C., Tassan-Got, L., Ketcham, R.A., and Dobson, K.J., 2012, Accounting for long alpha-particle stopping distances in (U-Th-Sm)/He geochronology: 3D modeling of diffusion, zoning, implantation, and abrasion: Geochimica et Cosmochimica Acta, v. 96, p. 44–56, <https://doi.org/10.1016/j.gca.2012.08.016>.
- Gehrels, G., and Pecha, M., 2014, Detrital zircon U-Pb geochronology and Hf isotope geochemistry of Paleozoic and Triassic passive margin strata of western North America: Geosphere, v. 10, p. 49-65.
- Gehrels, G.E., Valencia, V.A., and Ruiz, J., 2008, Enhanced precision, accuracy, efficiency, and spatial resolution of U-Pb ages by laser ablation–multicollector–inductively coupled

- plasma–mass spectrometry: *Geochemistry, Geophysics, Geosystems*, v. 9, Q03017, <https://doi.org/10.1029/2007GC001805>.
- Gleadow, A.J.W., Hurford, A.J., and Quaife, R.D., 1976, Fission track dating of zircon: Improved etching techniques. *Earth and Planetary Science Letters* v. 33, p. 273–276.
- He, J.J.Y., and Reiners, P.W., 2022, A revised alpha-ejection correction calculation for (U–Th)/He thermochronology dates of broken apatite crystals: *Geochronology*, v. 4, p. 629–640, <https://doi.org/10.5194/gchron-4-629-2022>.
- He, J.J.Y., Thomson, S.N., Reiners, P.W., Hemming, S.R., and Licht, K.J., 2021, Rapid erosion of the central Transantarctic Mountains at the Eocene-Oligocene transition: Evidence from skewed (U–Th)/He date distributions near Beardmore Glacier: *Earth and Planetary Science Letters*, v. 567, 117009, <https://doi.org/10.1016/j.epsl.2021.117009>.
- Hurford, A.J., and Green, P.F., 1983, The zeta age calibration of fission-track dating: *Chemical Geology*, v. 41, p. 285–317.
- Ketcham, R.A., Carter, A., Donelick, R.A., Barbarand, J., and Hurford, A.J., 2007, Improved modeling of fission-track annealing in apatite: *American Mineralogist*, v. 92, p. 799-810, <https://doi.org/10.2138/am.2007.2281>
- Kuiper, K.F., Deino, A., Hilgen, F.J., Krijgsman, W., Renne, P.R., and Wijbrans, J.R., 2008, Synchronizing rocks clocks of Earth history: *Science*, v. 320, p. 500-504.
- Lee, J.-Y., Marti, K., Severinghaus, J.P., Kawamura, K., Yoo, H.-S., Lee, J.B., and Kim, J.S., 2006, A redetermination of the isotopic abundances of atmospheric Ar. *Geochimica et Cosmochimica Acta*, v. 70, p. 4507-4512.
- Min, K., Mundil, R., Renne, P.R., and Ludwig, K.R., 2000, A test for systematic errors in $^{40}\text{Ar}/^{39}\text{Ar}$ geochronology through comparison with U/Pb analysis of a 1.1-Ga rhyolite: *Geochimica et Cosmochimica Acta*, v. 64, p. 73-98.

- Paces, J.B., and Miller Jr, J.D., 1993, Precise U-Pb ages of Duluth complex and related mafic intrusions, northeastern Minnesota: Geochronological insights to physical, petrogenetic, paleomagnetic, and tectonomagmatic processes associated with the 1.1 Ga midcontinent rift system: *Journal of Geophysical Research: Solid Earth*, v. 98, p. 13997-14013.
- Pullen, A., Ibáñez-Mejía, M., Gehrels, G.E., Giesler, D., and Pecha, M., 2018, Optimization of a laser ablation-single collector-inductively coupled plasma-mass Spectrometer (Thermo Element 2) for accurate, precise, and efficient zircon U-Th-Pb geochronology: *Geochemistry, Geophysics, Geosystems*, v. 19, p. 3689-3705.
- Reiners, P.W., Carlson, R.W., Renne, P.R., Cooper, K.M., Granger, D.E., McLean, N.M., and Schoene, B., 2018, *Geochronology and Thermochronology*: Oxford, John Wiley and Sons Ltd., 464 p.
- Ritz, M., and Valášková, M., 2018, Infrared and Raman spectroscopy of three commercial vermiculites doped with cerium dioxide nanoparticles: *Spectrochimica Acta Part A: Molecular and Biomolecular Spectroscopy*, v. 201, p. 39-45, <https://doi.org/10.1016/j.saa.2018.04.053>.
- Ross, J., 2019, NMGR/psychron v18.2: Zenodo, <https://doi.org/10.5281/zenodo.3237834>.
- Spiegel, C., Kohn, B., Belton, D., Berner, Z., and Gleadow, A., 2009, Apatite (U-Th-Sm)/He thermochronology of rapidly cooled samples: the effect of He implantation: *Earth and Planetary Science Letters*, v. 285, p. 105–114, <https://doi.org/10.1016/j.epsl.2009.05.045>.
- Stacey, J.T., and Kramers, J., 1975, Approximation of terrestrial lead isotope evolution by a two-stage model: *Earth and planetary science letters*, v. 26, p. 207-221.
- Vermeesch, P., 2009, RadialPlotter: a Java application for fission track, luminescence and other radial plots: *Radiation Measurements*, v. 44, p. 409-410.
- Wang, A., Freeman, J.J., and Jolliff, B.L., 2015, Understanding the Raman spectral features of phyllosilicates: *Journal of Raman Spectroscopy*, <https://doi.org/10.1002/jrs.4680>.